Nuclear Materials and Energy 41 (2024) 101765

Contents lists available at ScienceDirect

Nuclear Materials and Energy

journal homepage: www.elsevier.com/locate/nme

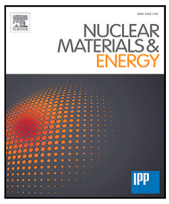

# Validating reduced models for detachment onset and reattachment times on MAST-U

S.S. Henderson [a,*], M. Bernert [b], D. Brida [b], G.L. Derks [d,e], S. Elmore [a], F. Federici [c], J.R. Harrison [a], A. Kirk [a], B. Kool [d,e], N. Lonigro [a,f], J. Lovell [c], D. Moulton [a], H. Reimerdes [g], P. Ryan [a], J.M. Stobbs [a], K. Verhaegh [a], T. van den Doel [d,e], T. Wijkamp [d], O. Bardsley [a], The MAST-U Team [1], The EUROfusion Tokamak Exploitation Team [2]

[a] United Kingdom Atomic Energy Authority, Culham Campus, Abingdon, OX14 3DB, UK
[b] Max Plank Institute for Plasma Physics, Boltzmannstr. 2, Garching 85748, Germany
[c] Oak Ridge National Laboratory, Oak Ridge, TN, 37831, USA
[d] Dutch Institute for Fundamental Energy Research, Eindhoven, The Netherlands
[e] Eindhoven University of Technology, Control Systems Technology, Eindhoven, The Netherlands
[f] York Plasma Institute, University of York, York, UK
[g] EPFL, Swiss Plasma Centre (SPC), Lausanne CH 1015, Switzerland

ARTICLE INFO

*Keywords:*
Detachment onset
Divertor reattachment
Impurity seeding
MAST upgrade

ABSTRACT

Two reduced models for predicting detachment onset and divertor reattachment times are validated on MAST Upgrade (MAST-U). These models are essential for future tokamak reactor design, providing rapid calculations based primarily on engineering parameters. The first model predicts detachment onset using a qualifier developed on ASDEX Upgrade (AUG) and later tested on JET, while the second model provides an estimate for the time required for a given transient to burn through the neutral particles in the divertor. Experiments in H-mode plasma scenarios were conducted on MAST-U with double-null and single-null configurations, which involved $D_2$ fuelling ramps and $N_2$ seeding. The detachment onset was determined by monitoring divertor parameters, including the target heat flux profile, electron temperature, and electron density, with measurements showing consistency with AUG-derived predictions. Reattachment times were assessed during dynamic vertical shifts of the plasma centroid position, with observations indicating reattachment within milliseconds, consistent with model predictions. Overall, the results confirm the applicability of both reduced models to MAST-U, extending their validation beyond AUG and JET.

## 1. Introduction

Designing future power plant reactors is a major focus in fusion research [1]. Low-fidelity, or reduced, models are crucial for identifying possible operational points for fusion reactors due to their rapid calculation times [2]. Reduced models usually have the benefit of being tested over a broad domain, either because they are inherently built on multi-machine database regressions or because they can be more readily applied across larger datasets. Consequently, they can also serve as a coarse consistency check for high-fidelity simulations. Given the significant technological gap between current tokamak research experiments and future burning tokamaks, validating reduced and high-fidelity models remains critical. Data-driven models are valid within the range of interpolation. To extend their application to extrapolation, evidence must be provided to demonstrate their accuracy beyond the original data range. This paper aims to validate two reduced models for predicting detachment access and divertor reattachment burn-through times.

Divertor detachment is crucial for ensuring that future integrated reactor plasma scenarios are compatible with tolerable heat loads and levels of erosion within the divertor region [3]. Moreover, a divertor detachment control system is essential for managing transient events, such as fluctuations in power crossing the separatrix or towards the individual divertors, changes in density in the divertor region, or even failures in impurity gas or pellet injection systems [4,5]. Predicting the time required to ionise, or 'burn-through', the volume of neutrals

* Corresponding author.
*E-mail address:* stuart.henderson@ukaea.uk (S.S. Henderson).
[1] See the author list of J. Harrison et al 2019 Nucl. Fusion 59 112011.
[2] See the author list of E. Joffrin et al 2024 Nucl. Fusion 64 112019.

https://doi.org/10.1016/j.nme.2024.101765
Received 4 July 2024; Received in revised form 15 September 2024; Accepted 8 October 2024
Available online 16 October 2024

in front of the target plate during a given power transient is critical for establishing the allowable response time in the control system. The remaining challenge lies in accurately predicting the timescales associated with various power transients and determining whether the steady-state detachment solution can be optimised to increase the burn-through time. Ideally, the burn-through becomes so large that the neutral volume never fully ionises over the transient timescale, allowing the expected transients to be absorbed passively.

Detachment access is predicted using a simple qualifier developed on ASDEX Upgrade (AUG) [6,7]:

$$q_{\mathrm{det}} = 1.3 \frac{P_{\mathrm{sep}}/R_{\mathrm{maj}}\,(5\mathrm{mm}/\lambda_{\mathrm{int}})}{p_0\,(1+f_Z c_Z)} \left(\frac{1.65\ \mathrm{m}}{R_{\mathrm{maj}}}\right)^{0.1}. \quad (1)$$

The numerator parameters in the first ratio arise due to the dependence on the parallel energy flux density, where $P_{\mathrm{sep}}$ is the power crossing the separatrix, $R_{\mathrm{maj}}$ is the major radius, and $\lambda_{\mathrm{int}}$ is the power decay width including broadening. The denominator is associated with the power dissipation through momentum and radiation loss, where $p_0$ is the divertor neutral pressure, $c_Z$ is an average scrape-off layer (SOL) impurity concentration, and $f_Z$ is a factor describing the impurities ability to radiate relative to deuterium, e.g. for nitrogen $f_{\mathrm{N}} = 18$. The ratio in brackets appears due to the weak scaling with connection length. The factor 1.3 is used so that $q_{\mathrm{det}} = 1$ indicates partial detachment on AUG, defined as a significant reduction of heat flux and pressure along field lines between the midplane and divertor target within a power decay length in the SOL. The same factor is used in MAST-U, AUG, and JET, however further generalisations are used for MAST-U as discussed in Section 2.1.

The time taken to burn-through the neutrals is described by a static relation developed on AUG [8]:

$$t^{\mathrm{B-T}} = 0.09 \sqrt{\left(\frac{p_0}{2\mathrm{Pa}}\right)\left(\frac{n_{\mathrm{e}}}{3\times10^{20}\ \mathrm{m}^{-3}}\right)\left(\frac{V}{0.4\ \mathrm{m}^3}\right)\left(\frac{L_{\mathrm{f}}}{12\ \mathrm{m}}\right)\left(\frac{t^{\mathrm{max}}}{0.2\ \mathrm{s}}\right)\left(\frac{2.67\ \mathrm{MW}}{\Delta P}\right)}.$$

$V$ is an estimate of the volume of neutrals in front of the target, $L_{\mathrm{f}}$ is the connection length between the detachment front location and target (originally denoted by $L_X$ for X-point radiators on AUG) normalised by the value found in the flux surface ≈ 1 mm away from the separatrix on AUG, $n_{\mathrm{e}}$ is the electron density in the divertor region normalised by the average value determined by spectroscopic Stark broadening measurements, and $t^{\mathrm{max}}$ and $\Delta P$ denote the total duration and magnitude of the power transient, respectively. The formula is derived by assuming a linearly increasing power, $P(t) = t\Delta P/t^{\mathrm{max}}$, and a constant divertor neutral pressure during the power transient.

Previous studies have tested these two reduced models on AUG and JET, in single-null configuration with vertical–vertical inner–outer divertor geometry [6–9]. The experiments assessed mixtures of N, Ne, and Ar impurity gases and applied both impurity gas cuts and step increases of the neutral beam injection power up to 5 MW during phases of deep detachment. Validation is now extended to ELMy H-mode MAST-U plasma scenarios, which feature both single-null and double-null configuration with significantly different divertor geometry to both AUG and JET.

The paper is structured as follows: Section 2 presents a description of the MAST-U H-mode plasma scenario, incorporating fuelling ramps and $N_2$ seeding. This section also includes the validation of the detachment qualifier. Section 3 provides an overview of the power transients induced in the H-mode plasma scenario by variations in the vertical position of the plasma centroid, along with an assessment of the detachment front burn-through time. Finally, the conclusions are given in Section 4.

## 2. Assessment of detachment onset

Detachment onset is assessed on MAST-U using a double-null H-mode plasma with plasma current $I_{\mathrm{P}} = 0.75$ MA, toroidal field on axis $B_0 = 0.55$ T, neutral beam injection power $P_{\mathrm{NBI}} = 3.4$ MW, and major and minor radii $R_{\mathrm{maj}} = 1$ m and $a_{\mathrm{min}} = 0.55$ m, respectively. The machine geometry is shown in Fig. 1, featuring a vertical–horizontal inner–outer divertor geometry and outer target strike-point at a 'conventional' location (i.e., $R_{\mathrm{t,outer}} \approx R_{\mathrm{maj}}$).

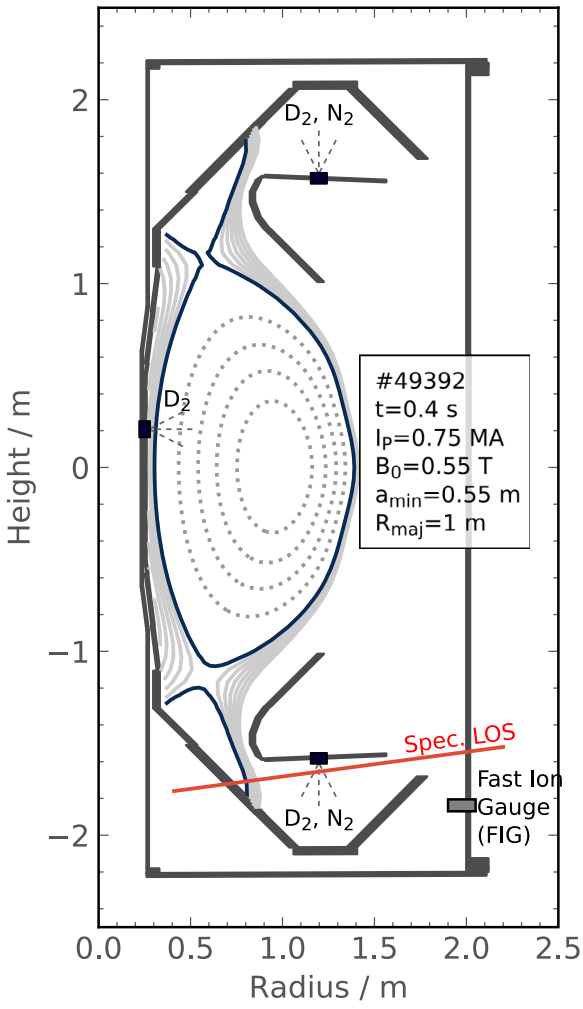


**Fig. 1.** The machine geometry and magnetic equilibrium of the reference H-mode scenario used to determine the detachment onset.

The plasma time traces for the reference scenario #49392 are shown by the navy lines in Fig. 2. Regular ELMs are occur throughout most of the scenario. $H_{98(y,2)}$ is typically less than 1 in most MAST-U H-mode scenarios. This is thought to be due to the formation of tearing modes (magnetic islands) which cause an increase in cross-field transport. Interactions with resistive-wall eddy currents and error fields can cause these tearing modes to lock, triggering a disruption [10,11]. A low level $D_2$ puff through the high-field side midplane valve during the H-mode phase results in a rising divertor pressure of $p_0 = 0.3$–$0.6$ Pa, as measured by the Fast Ion Gauge (FIG) located in the sub-divertor as shown in Fig. 1. The gas valve fluxes shown in Fig. 2 (and also later in 3) are requested flow rates and do not necessarily represent exactly the true injected flow rates.

To induce detachment, firstly the divertor pressure is raised by additional $D_2$ puffing through gas valves located within the upper and lower outer divertor chambers, as shown by the time traces in Fig. 2 for #49139 and #49270. The divertor pressure rises linearly with the applied $D_2$ puff up to a value of ≈ 1 Pa and > 1.45 Pa (the FIG saturates at ≈ 1.45 PA), respectively, in the two fuelling ramp scenarios shown. Midplane $D_\alpha$ emission increases in line with the $D_2$ puff and indicates

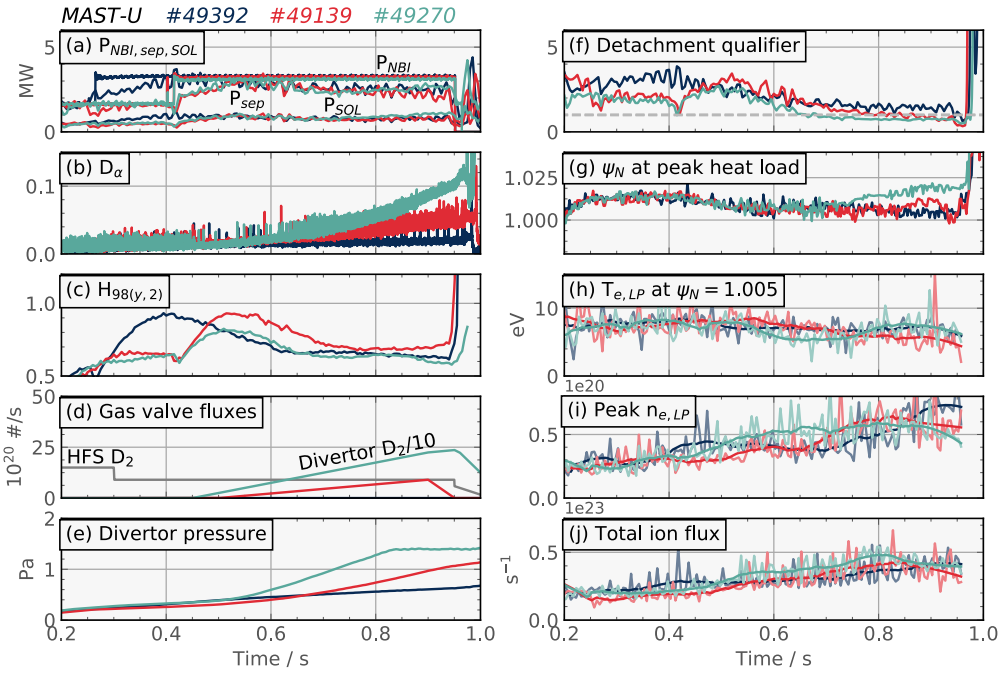


**Fig. 2.** Plasma time traces for the reference H-mode scenario #49392 and the fuelling ramp scans (#49139 and #49270) for detachment onset determination.

an increase in ELM frequency after the $D_2$ ramp begins. During this phase, the pedestal top temperature drops from ≈ 250 eV to ≈ 100 eV. A drop in peak $H_{98(y,2)}$ from ≈ 0.95 to ≈ 0.8 is found between the scenario with and without a fuelling ramp; however, $H_{98(y,2)}$ stabilises at ≈ 0.6–0.7 in all scenarios.

Next, the $D_2$ puff was replaced by both a ramp and a flat level of $N_2$ seeding from the same valve locations. Plasma time traces are shown in Fig. 3. It was necessary to move the outer strike-point ≈ 2 cm outwards in comparison to the $D_2$ scenario to help stabilise the scenario at higher $N_2$ seeding levels; however, at $N_2$ seeding rates of $\approx 2\times10^{21}$ atoms/s the MHD locks leading to a disruption. Whether this is inherently due to the impact of impurities on the MHD, or a result of an unstable MARFE is not yet clear. The pedestal behaviour following the $N_2$ injection is similar to the $D_2$ fuelled scenario, showing a drop in pedestal temperature and an increase in ELM frequency. Although the divertor pressure is rising during the seeding scenario, $N_2$ injection causes only a small change in divertor neutral pressure between the two scenarios.

The divertor $N$ concentration, $c_N$, is determined through visible spectroscopy using previously established methodology [12]. This method connects the $N$ II intensity measured along the line-of-sight (LOS), as shown in Fig. 1, with the $N$ concentration. The width of the $N$ II emission along the line-of-sight is ≈ 5 cm, based on the assumption that the emission originates within the near SOL of width $\lambda_{int}$ ≈ 1 cm with a flux expansion factor of ≈ 3, and extends 1–2 cm into the private flux region. Langmuir probe measurements at the outer target of $3.5–4.5\times10^{19}$ $m^{-3}$ (see Fig. 3i) are used to estimate the electron density associated with the emission region. This estimation is consistent with $N$ II line ratio measurements. Dashed lines represent the derived $c_N$ in Fig. 2d, indicating peak values between ≈ 25%–40%, with shaded regions illustrating the error due to a 20% uncertainty in electron density.

### 2.1. Divertor evolution

The detachment qualifier is generalised for this analysis by dividing Eq. (1) by the power fraction directed to the outer divertor on AUG, $f_{SOL} = f_{div} f_{wall} = 0.42$, which is derived from assuming two thirds of the power directed to the outer divertor $f_{div} = 0.66$ and a fraction $f_{wall} = 1 - 1/e$ lost to the wall [7,13], where $e$ is the base of the natural logarithm (≈ 2.718). The power to the outer target is then $P_{SOL} = P_{sep} f_{SOL}$. The $f_{div}$ fraction for MAST-U varies as a function of the distance between primary and secondary separatrices, $dr_{sep}$. In near connected double-null (i.e. $-1 < dr_{sep} < 1$ mm), $f_{div} \approx 0.45$ and, therefore, applying $f_{wall}$ as above, gives $f_{div} \approx 0.3$.

An overview of the relevant divertor time traces is shown in the plots on the right of Fig. 2 and Fig. 3. The calculated detachment qualifier in Fig. 2f and Fig. 3f is discussed first. The calculation assumes no intrinsic (i.e. carbon) impurity radiation, which is consistent with recent high-fidelity modelling MAST-U [14], though this remains an uncertainty in the analysis. $\lambda_q$ is measured to be ≈ 7 mm and $\lambda_{int}$ is estimated using $\lambda_{int} = \lambda_q + 1.64S$, where is $S$ is the SOL broadening term estimated as $\lambda_q/2$ [15].

To determine the point at which partial detachment occurs on MAST-U, data from both the Infra-Red (IR) diagnostic [16] and the Langmuir probes [17] are shown in Fig. 2g and Fig. 3g. The normalised poloidal flux surface $\psi_N$ corresponding to the peak heat load measured by IR indicates when the peak first moves away from the target into the SOL. In both fuelling and seeding scenarios, there is a clear increase in $\psi_N$ coinciding with $q_{det} \approx 1$.

Next, the electron temperature at the target, $T_{e,LP}$, determined by the probe located closest to $\psi_N = 1.005$, is shown in Fig. 2h and Fig. 3h. High-frequency ELMs make the interpretation challenging, so smoothing is applied for clarity and indicates a drop in $T_{e,LP}$ to ≈ 5 eV as $q_{det}$ approaches unity. While the peak temperature measured by the Langmuir probes drops to ≈ 5 eV at the onset of detachment, it does not fall below this value beyond the detachment point. This could be attributed to the challenges in interpreting probe characteristics in detached plasmas. Alternatively, frequent ELM burn-through in H-mode may prevent the steady-state temperature from dropping significantly below ≈ 5 eV.

The next panels in Fig. 2i and Fig. 3i show the peak electron density measured across the entire target, $n_{e,LP}$. A roll-over in electron density is typically associated with detachment due to the loss in momentum along the flux surface and strong electron-ion recombination near the target [18] and is observed clearly for the seeding scenarios. The roll-over is less pronounced for the fuelling scenarios, which could be due to

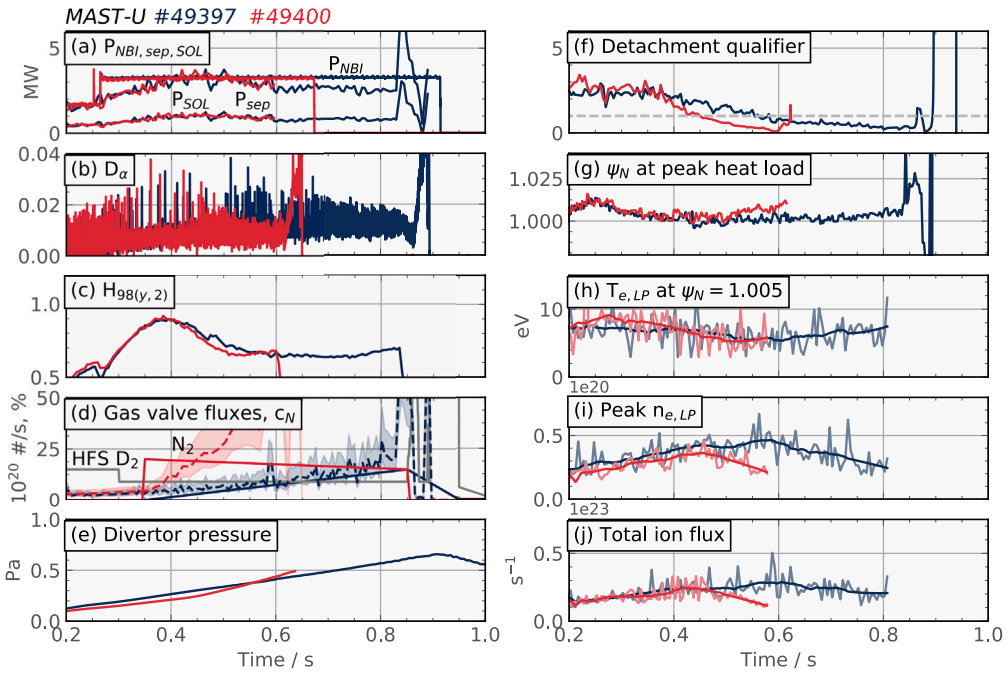


**Fig. 3.** Plasma time traces for the two H-mode scenarios with $N_2$ seeding (#49397 and #49400) used for detachment onset determination.

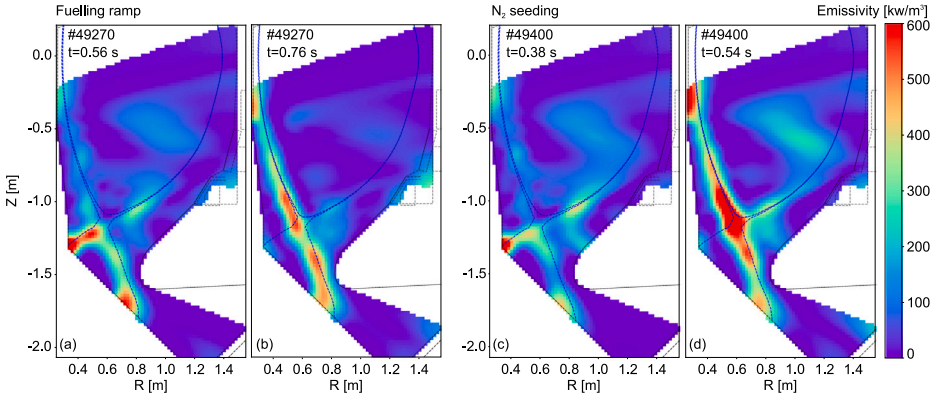


**Fig. 4.** Poloidal inversions of the total emissivity measured by the infrared video bolometer on MAST-U for both the fuelling and seeding scenarios.

the injected gas flux being of similar magnitude to the target recycling flux. For clarity, the total ion flux to the outer target measured by the probes is shown in Fig. 2j and Fig. 3j and shows a similar roll-over as found for the peak electron density.

Poloidal inversions of the total emissivity measured by the infrared video bolometer (IRVB) diagnostic [19,20] are shown in Fig. 4. The panels show one time slice before partial detachment (Figs. 4a and c) and one time slice after partial detachment occurs (Figs. 4b and d) for the fuelling and seeding scenarios, respectively. Before partial detachment occurs, the emission is strongly localised at both the inner and outer divertors. After partial detachment of the outer divertor occurs, the emission is no longer localised at the inner divertor, and the emission around the outer divertor spreads upstream from the target to the X-point. However, since there is still a non-negligible amount of radiation observed at the outer target, this likely indicates that pronounced detachment has not yet been achieved. Significant radiation is observed on the high-field side (HFS) region up to the midplane as the outer divertor detaches. This is often associated with a MARFE [21] and could be driven unstable by the inherently low power available on the HFS in double-null configuration.

Table 1 summarises the parameter ranges over which the detachment qualifier has been tested. While a wide range has been tested in each parameter, reactor scenarios will operate at higher divertor pressures (10–20 Pa) and higher $P_{sep}/R_{maj} > 20$ MWm$^{-1}$.

**Table 1**
Parameter ranges over which the detachment qualifier has been tested. Impurity concentrations are derived from spectroscopic measurements of the outer divertor.

| Parameter | AUG | JET | MAST-U |
|---|---|---|---|
| $P_{sep}/R_{maj}$ MWm$^{-1}$ | 3 – 10 | 3 – 7 | 2.5 – 3 |
| $\lambda_q$ mm | ≈ 2 | ≈ 2 | ≈ 7 |
| $p_0$ Pa | 0.8 – 2.5 | ≈ 1.5 | 0.3 – 1.5 |
| $c_N$ % | < 20 | < 20 | < 25 |
| $c_{Ne}$ % | < 1 | < 5 | – |
| $c_{Ar}$ % | < 1 | < 2 | – |

## 3. Divertor reattachment times

Currently, with only two NBI systems available on MAST-U, and typically both beams are required for high performance scenarios, increasing power by NBI is not feasible. The most straightforward technique to induce a power transient in MAST-U is to vertically shift the plasma from a near-connected double-null to a lower single-null configuration. In this scenario, the power to the outer divertor increases

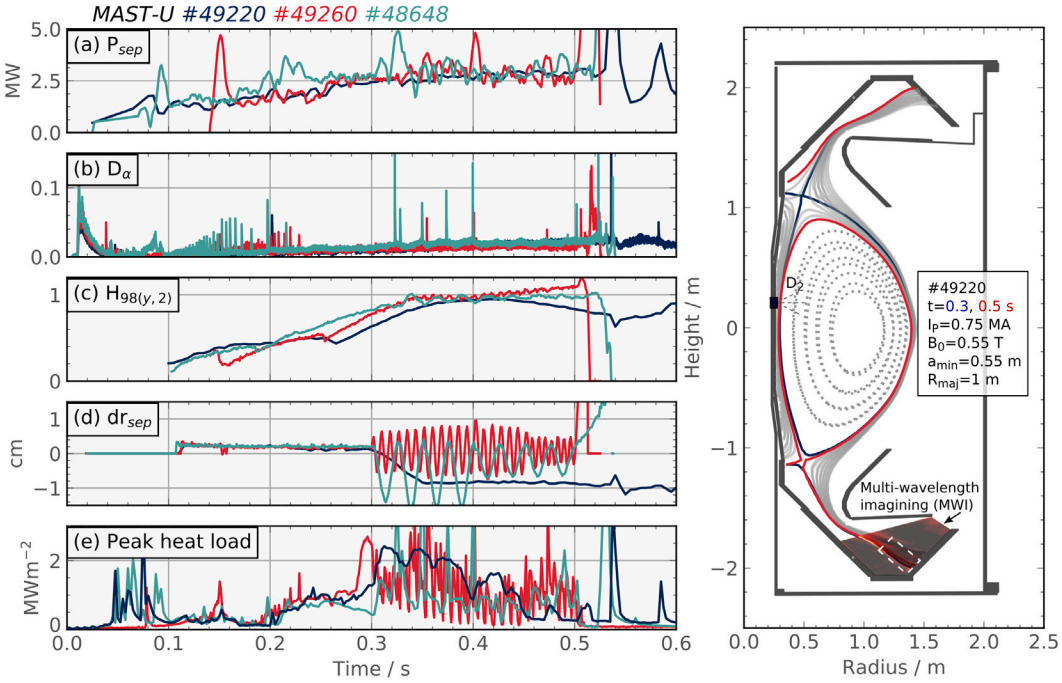


**Fig. 5.** Lower single-null (#49220) and dynamic double-null (#49260 and #49648) H-mode scenarios on MAST-U.

approximately by a factor two in lower single-null (i.e. $dr_{\mathrm{sep}}/\lambda_{\mathrm{q}} > -1$) while the power to the inner target increases by roughly a factor three [22]. Finally, because the conventional divertor is difficult to detach, a super-X divertor configuration was chosen, which is typically strongly detached in double-null H-mode MAST-U scenarios. The super-X configuration also benefits from wider diagnostic coverage, facilitating to burn-through measurements.

The plasma time traces and machine geometry are shown in Fig. 5. In all scenarios, the super-X configuration is established by $t = 0.3$ s, with a vertical–horizontal inner–outer geometry and outer target strike-point positioned at $R_{\mathrm{t,outer}} \approx R_{\mathrm{maj}} + a_{\mathrm{min}}$. Three scenarios are shown: #49220 features a near connected double-null scenario with a relatively slow transition to lower single-null (referred to as steady-state LSN) occurring between $t = 0.3 - 0.35$, while #49260 and #49648 are double-null scenarios with oscillations in vertical position at frequencies of 120 Hz and 40 Hz, respectively, at varying perturbation amplitudes starting at $t = 0.3$ s (denoted dynamic DN). Overall, oscillation frequencies were tested up to and including 200 Hz. A $dr_{\mathrm{sep}} \approx -1$ cm in steady-state LSN, corresponding to a $\approx -10$ cm shift in the vertical plasma centroid, is the limit before the plasma transitions back into L-mode. Oscillation amplitudes greater than $dr_{\mathrm{sep}} \approx -1$ cm typically trigger large ELMs, as shown by #48648 in Fig. 5.

IR measurements indicate an inward shift of the lower outer strike-point by up to 5 cm during the downward movement of the plasma. This shift may reduce the time required to burn through the detachment front by decreasing the connection length. However, the shift represents less than a 5% change in the strike-point position and is therefore assumed to have a relatively small impact on the overall uncertainty in validating the burn-through time predictions.

The steady-state LSN scenario results in an ELM-free H-mode, with $H_{98(y,2)}$ approaching unity and then reducing to $\approx 0.8$. Intriguingly, both dynamic DN scenarios have $H_{98(y,2)}$ above one for the full duration of the scenario. However, both dynamic DN scenarios are cut short by disruptions occurring at $t \approx 0.52$ s. The peak heat loads measured at the lower outer divertor by IR show an increase up to $\approx 2$ MWm$^{-2}$ during the transition to steady-state LSN, with the divertor reattaching to the target, while the loads oscillate between noise levels and $\approx 2$ MWm$^{-2}$ in the dynamic DN scenarios. The average peak heat load in all three scenario decreases from $t > 0.35$ s due to the rising divertor pressure.

The divertor detaches at $\approx 0.4$ s in the steady-state LSN scenario. A preliminary evaluation of the detachment qualifier indicates values around 3.5 at this time, despite the divertor being detached. This discrepancy may stem from two missing factors. First, the detachment qualifier may need to account for total flux expansion, which could be addressed by replacing $P_{\mathrm{sep}}/R_{\mathrm{maj}}$ with $P_{\mathrm{sep}}/R_{\mathrm{t,outer}}$. Second, the detachment qualifier may require an additional correction factor to scale the divertor pressure and account for differences in the ratio between the divertor and sub-divertor neutral pressures. For instance, using $R_{\mathrm{t,outer}} =\approx 1.3$ m instead of $R_{\mathrm{maj}} \approx 0.8$ m and assuming the neutral pressure in the divertor is approximately twice as high as in the sub-divertor in the super-X configuration, the detachment qualifier more accurately predicts the detachment threshold. Another possibility is that the divertor broadening, $\lambda_{\mathrm{int}}$, is stronger in super-X configuration compared to conventional configuration. Finally, the influence of the inner target on the outer target's detachment threshold may also differ in the super-X configuration. These hypotheses warrant further investigation through high-fidelity modelling and will be explored in future work.

### 3.1. Divertor evolution

The divertor evolution for the four oscillations during #48648 between $t = 0.4$–$0.5$ s are shown in Fig. 6, with the time axis normalised to the beginning of the downward oscillation in each case. In each panel, red symbols indicate the lower outer divertor values averaged over all oscillations, while blue symbols, if present, represent the equivalent values in the upper outer divertor. The top panel illustrates the evolution of the power directly driven to the outer target, calculated using a parameterised form of power sharing as a function of $dr_{\mathrm{sep}}$ to match results from SOLPS-ITER modelling (see Fig. 3 of [23]). Next, the location of the lower outer divertor deuterium Fulcher band emission, measured by the multi-wavelength imaging (MWI) diagnostic [24], is shown, expressed as the distance from the emission front edge to the

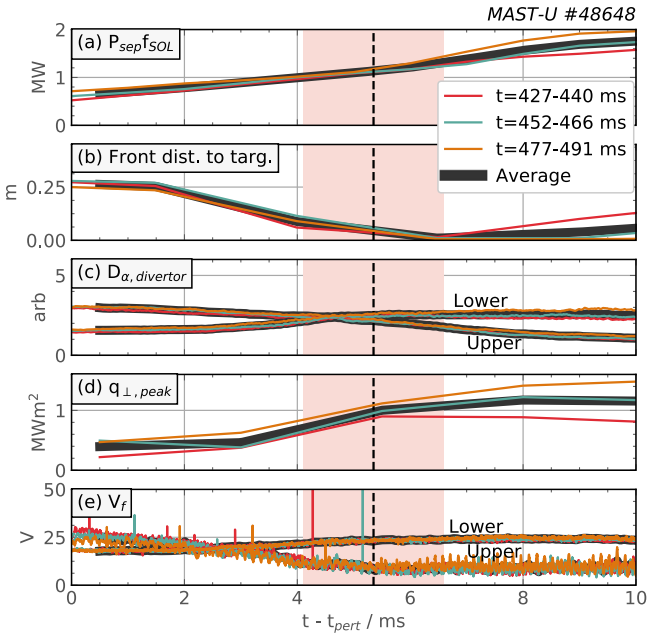


**Fig. 6.** Summary of divertor neutral burn-through measurements. See text for details.

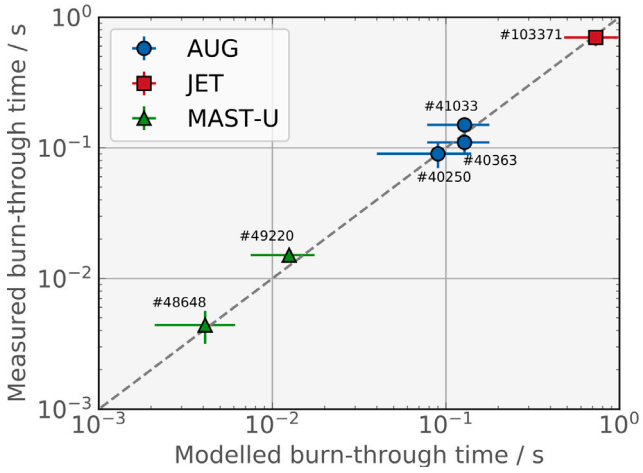


**Fig. 7.** Multi-machine comparison of modelled and measured detachment front burn-through times. The device shot numbers used to calculate the data are provided.

target along the divertor leg. The vertical dashed line marks the time when the front reaches the target. The shaded region indicates the uncertainty, which is determined by the diagnostic time resolution. In the case shown, the derived time for burn-through is $t^{B-T} = 5.4 \pm 1.3$ ms.

The next panels in Fig. 6 further demonstrate the divertor evolution during the oscillations. Firstly, the divertor $D_\alpha$ emission shows that, before the oscillation begins (i.e. in double-null), the upper divertor $D_\alpha$ is brighter than the lower divertor, with the balance in emission inverting as the plasma moves into lower single-null. The peak heat loads from IR measurements in the lower divertor begin at noise level and then increase up to $\approx$ 1 MWm$^{-2}$. Finally, the floating potential, $V_f$ measured by the probes, which partly depends on the electron temperature, shows a weak rise in the lower divertor and a more pronounced drop in the upper divertor.

The measured peak heat load in the lower outer divertor does not show any significant change until $\approx$ 3 ms after the transient, just prior to the front reaching the target. Conversely, the $D_\alpha$ and $V_f$ in the upper divertor are changing after $\approx$ 1 ms. A delay in the global response of the divertor can be caused by dynamics of the applied power perturbation. A sinusoidal perturbation, as used in the dynamic DN scenarios, introduces a natural delay time not accounted for in Eq. due to assuming a linearly increasing power transient. For example, in the scenario shown with a 40 Hz sine wave perturbation, the power distribution changes by $<$ 2% over 1 ms at the beginning of the transient, compared to $\approx$ 10% for an equivalent linear perturbation. These dynamics likely explain the observed $\approx$ 1 ms delay before the upper divertor $D_\alpha$ signal begins to reduce, and the 1 ms delay before the detachment front position in the lower divertor begins to move. Thus, 1 ms is also subtracted from the experimental burn-through time.

The relatively longer delay of $\approx$ 3.3 ms observed before the peak heat load begins to rise in the lower divertor, in comparison to the 1 ms discussed above, is consistent with observations on AUG which showed a delay of $\approx$ 100 ms before the divertor temperature began to rise after a step increase of NBI power was applied to an X-point radiator scenario [8]. This study on AUG also demonstrated that, for the same power perturbation, a scenario with a partially detached outer divertor exhibited an almost instantaneous rise in divertor temperature. This suggests that ITER, which is expected to operate in the partial detachment regime, may require highly efficient actuators capable of influencing the SOL plasma at least as quickly as the anticipated SOL transient time scale to avoid reattachment. Reactors operating under strongly detached conditions may benefit from implementing early warning detachment systems to pre-emptively avoid reattachment.

To calculate the predicted burn-through time using Eq. , the relevant parameters are determined to be $t^{max} = 9$ ms (accounting for the 1 ms delay in the sinusoid perturbation), $\Delta P = 1$ MW (derived from Fig. 5a), $p_0 = 0.4$ Pa, $n_e = 5 \times 10^{19}$ m$^{-3}$, $L_f \approx 4$ m (estimated from $R \approx 1$ m), and $V = 2\pi R A_{pol} \approx 0.6$ m$^3$. Defining the volume of neutrals accurately is challenging; it is currently estimated using a rectangular box, as indicated by the white dashed lines in the equilibrium shown in Fig. 5. A systematic approach to defining the dimensions of this box was attempted by setting its poloidal width to $5\lambda_{int} f_x \approx 0.3$ (consistent with the original AUG case), where $f_x$ represents the poloidal flux expansion. The poloidal height was defined as $\approx$ 0.25 which was determined from the poloidal distance between the target and detachment front location. This approach results in $A_{pol} \approx 0.08$ m$^2$ and $R \approx 1.3$ m. Using these parameters gives a predicted time of $t^{B-T} \approx 4.1$ ms. After subtracting 1 ms from the experimentally determined burn-through time of 5.4 $\pm$ 1.3 ms, a predicted value of 4.1 ms is well within the experimental value of 4.4 $\pm$ 1.3 ms.

In the steady-state LSN scenario, there is a linear change in the plasma vertical position over 50 ms. Burn-through in this scenario occurs within $t^{B-T} \approx 15 \pm 1.25$ ms, while the model predicts a value of $t^{B-T} \approx 12$ ms. Similar to the case shown in Fig. 5, the peak heat loads start to rise $\approx$ 9 ms after the transient, just before the front reaches the target.

Providing an absolute uncertainty for the modelled burn-through time is challenging. Factors such as the volume of neutrals are only estimations. The focus should be on using the simplified estimations to understand parameter scaling both across different machines and within a single device. To visualise the uncertainty from two of the most uncertain parameters, the volume and electron density, an uncertainty is defined by using $V \pm 50$ % and $n_e \pm 20$ %. A comparison of burn-through times across AUG, JET, and MAST-U is shown in Fig. 7. The burn-through time for #49260 could not be calculated due to the unavailability of MWI measurements for this discharge. The predictions generally align with the measured burn-through times across the three devices, either within the measurement or prediction uncertainty.

These findings suggest that higher divertor neutral pressure may slow reattachment. Future experiments should assess whether burn-through time changes when the same power transient and detachment front location are applied, but detachment is induced either by impurity

seeding with low divertor pressure or high divertor pressure with low seeding. This would clarify if divertor neutral pressure directly affects burn-through time or if higher impurity concentration allows greater power dissipation through enhanced radiation during a power increase.

## 4. Conclusions

The detachment qualifier developed on AUG has now been tested in three different machines: AUG, JET, and MAST-U. Future experiments should prioritise validating the detachment qualifier in extended leg geometries and examining the impact of the toroidal field. Across these devices, the time taken to burn-through the neutrals in strongly detached conditions can be predicted using the static relation in Eq. .

Further validation of the burn-through time prediction model using data from additional machines would enhance confidence in its accuracy. However, the primary focus should now shift to testing parameter dependencies on a single machine, including factors such as the mixture of divertor pressure and impurity concentration, the position of the detachment front, the magnetic geometry of the divertor, and the electron density. Additionally, a simple model to predict the SOL impurity radiation should be developed and tested to better estimate the power available for neutral ionisation.

In summary, while further testing is still necessary, it is notable that such simplified models match different devices with parameters spanning orders of magnitude difference.

## CRediT authorship contribution statement

**S.S. Henderson:** Writing – original draft, Formal analysis, Data curation. **M. Bernert:** Writing – review & editing, Data curation. **D. Brida:** Data curation. **G.L. Derks:** Writing – review & editing, Formal analysis, Data curation. **S. Elmore:** Data curation. **F. Federici:** Formal analysis. **J.R. Harrison:** Data curation. **A. Kirk:** Formal analysis. **B. Kool:** Writing – review & editing, Formal analysis, Data curation. **N. Lonigro:** Formal analysis. **J. Lovell:** Formal analysis, Data curation. **D. Moulton:** Writing – review & editing, Formal analysis. **H. Reimerdes:** Data curation. **P. Ryan:** Formal analysis. **J.M. Stobbs:** Formal analysis. **K. Verhaegh:** Formal analysis. **T. van den Doel:** Formal analysis. **T. Wijkamp:** Formal analysis. **O. Bardsley:** Formal analysis.

## Declaration of competing interest

The authors declare that they have no known competing financial interests or personal relationships that could have appeared to influence the work reported in this paper.

## Acknowledgements

This work has been carried out within the framework of the EUROfusion Consortium, funded by the European Union via the Euratom Research and Training Programme (Grant Agreement No 101052200 - EUROfusion) and from the EPSRC [grant number EP/W006839/1]. The Swiss contribution to this work has been funded by the Swiss State Secretariat for Education, Research and Innovation (SERI). To obtain further information on the data and models underlying this paper please contact PublicationsManager@ukaea.uk. Views and opinions expressed are however those of the author(s) only and do not necessarily reflect those of the European Union, the European Commission or SERI. Neither the European Union nor the European Commission nor SERI can be held responsible for them.

## Data availability

Data will be made available on request.

## References

[1] N. Asakura, K. Hoshimo, S. Kakudate, F. Subba, J. You, S. Wiesen, T. Rognlien, R. Ding, S. Kwon, Nucl. Mater. Ener. 35 (2023) 101446.
[2] M. Siccinio, E. Fable, K. Lackner, A. Scarabosio, R. Wenninger, H. Zohm, Plasma Phys. Control. Fusion 58 (2016) 125011.
[3] R. Wenninger, R. Albanese, R. Ambrosino, F. Arbeiter, J. Aubert, C. Bachman, L. Barbato, T. Barrett, M. Beckers, W. Biel, Nucl. Fusion 57 (2017) 046002.
[4] S. Wiesen, F. Kochl, P. Belo, V. Kotov, A. Loarte, V. Parail, G. Corrigan, L. Garzotti, D. Harting, Nucl. Fusion 57 (2017) 076020.
[5] M. Siccinio, W. Biel, M. Cavedon, E. Fable, G. Federici, F. Janky, H. Lux, F. Maviglia, J. Morris, F. Palermo, O. Sauter, F. Subba, H. Zohm, Fusion Eng. Design. 156 (2020) 111603.
[6] A. Kallenbach, M. Bernert, M. Beurskens, L. Casali, M. Dunne, T. Eich, L. Giannone, A. Herrmann, M. Maraschek, S. Potzel, F. Reimold, V. Rohde, J. Schweinzer, E. Viezzer, M. Wischmeier, ASDEX Upgrade Team, Nucl. Fusion 55 (2015) 053026.
[7] A. Kallenbach, M. Bernert, R. Dux, F. Reimold, M. Wischmeier, Plasma Phys. Control. Fusion 58 (2016) 045013.
[8] S. Henderson, M. Bernert, D. Brida, M. Cavedon, P. David, R. Dux, O. Fevrier, A. Jarvinen, A. Kallenbach, Nucl. Fusion 63 (2023) 086024.
[9] S. Henderson, M. Bernert, D. Brida, M. Cavedon, P. David, R. Dux, O. Fevrier, P. Jacquet, A. Jarvinen, A. Kallenbach, J. Karhunen, K. Kirov, M.K.M. Lennholm, B. Lomanowski, C. Lowry, R. McDermott, A. Meigs, H. Reimerdes, H. Sun, B. Thomas, Nucl. Fusion 64 (2024) 066006.
[10] R. Sweeney, W. Choi, M. Austin, M. Brookman, V. Izzo, M. Knolker, R.L. Haye, A. Leonard, E. Strait, F. Volpe, Nucl. Fusion 58 (2018) 056022.
[11] A. Thornton, S. Gibson, C. Ham, A. Kirk, J. Harrison, R. Scannell, D. Battaglia, IAEA FEC 2023, London. 2023.
[12] S. Henderson, M. Bernert, S. Brezinsek, M. Carr, M. Cavedon, R. Dux, B. Lipschultz, M. OMullane, F. Reimold, M. Reinke, Nucl. Fusion 58 (2017) 016047.
[13] S. Henderson, M. Bernert, C. Giroud, D. Brida, M. Cavedon, P. David, R. Dux, J. Harrison, A. Huber, A. Kallenbach, J. Karhunen, B. Lomanowski, G. Matthews, A. Meigs, R. Pitts, F. Reimold, M. Reinke, S. Silburn, N. Vianello, S. Wiesen, M. Wischmeier, Nucl. Mater. Ener. 28 (2021) 101000.
[14] D. Moulton, J. Harrison, L. Xiang, P. Ryan, A. Kirk, K. Verhaegh, T. Wijkamp, F. Federici, J. Clark, B. Lipschultz, Nucl. Fusion 64 (2024) 076049.
[15] T. Eich, A. Leonard, R. Pitts, W. Fundamenski, R. Goldston, T. Gray, A. Herrmann, A. Kirk, A. Kallenbach, O. Kardaun, A. Kukushkin, B. LaBombard, R. Maingi, M. Makowski, A. Scarabosio, B. Sieglin, J. Terry, A. Thornton, Nucl. Fusion 53 (2013) 093031.
[16] J. Stobbs, Rev. Sci. Instrum. (2024) in review.
[17] P. Ryan, S. Elmore, J. Harrison, J. Lovell, R. Stephen, Rev. Sci. Instrum. 94 (2023) 103501.
[18] S. Krasheninnikov, A. Kukuskin, J. Plasma Physics 83 (2017) 155830501.
[19] F. Federici, M. Reinke, B. Lipschultz, A. Thornton, J. Harrison, J.J. Lovell, M. Bernert, Rev. Sci. Instrum. 94 (2023) 033502.
[20] F. Federici, M. Reinke, B. Lipschultz, J.J. Lovell, K. Verhaegh, C. Cowley, M. Kryjak, P. Ryan, A. Thornton, J. Harrison, B. Peterson, J. Lore, Y. Damizia, Nucl. Mater. Ener. submitted (2024).
[21] B. Lipschultz, B. LaBombard, E. Marmar, M. Pickrell, J. Terry, R. Watterson, S. Wolfe, Nucl. Fusion 24 (1984) 977.
[22] G.D. Temmerman, A. Kirk, E. Nardon, P. Tamain, J. Nucl. Mater. 415 (2011) S383–S386.
[23] R. Osawa, D. Moulton, S. Newton, S. Henderson, B. Lipschultz, A. Hudoba, Nucl. Fusion 63 (2023) 076032.
[24] T. Wijkamp, J. Allcock, X. Feng, B. Kool, B. Lipschultz, K. Verhaegh, B. Duval, J. Harrison, L. Kogan, N. Lonigro, A. Perek, P. Ryan, R. Sharples, I. Classen, R. Jaspers, Nucl. Fusion 63 (2023) 056003.